MATERIALS SCIENCE

Covalent organic frameworks with Ni-Bis(dithiolene) and Co-porphyrin units as bifunctional catalysts for Li-O_2 batteries

Si-Wen Ke[1]†, Wei Li[2]†, Yuming Gu[1]†, Jian Su[1], Yifan Liu[1], Shuai Yuan[1], Jing-Lin Zuo[1]*, Jing Ma[1]*, Ping He[2]*

The rational design of efficient and stable catalysts for the oxygen reduction reaction and oxygen evolution reaction (ORR/OER) is the key to improving Li-O_2 battery performance. Here, we report the construction of ORR/OER bifunctional cathode catalysts in a covalent organic framework (COF) platform by simultaneously incorporating Ni-bis(dithiolene) and Co-porphyrin units. The resulting bimetallic Ni/Co-COF exhibits high surface area, fairly good electrical conductivity, and excellent chemical stability. Li-O_2 batteries with the Ni/Co-COF–based cathode show a low discharge/charge potential gap (1.0 V) and stable cycling (200 cycles) at a current density of 500 mA g^{-1}, rivaling that of PtAu nanocrystals. Density functional theory computations and control experiments using nonmetal or single metal–based isostructural COFs reveal the critical role of Ni and Co sites in reducing the discharge/charge overpotentials and regulating the Li_2O_2 deposition. This work highlights the advantage of bimetallic COFs in the rational design of efficient and stable Li-O_2 batteries.

INTRODUCTION

Li-O_2 batteries are considered promising candidates for next-generation energy storage devices owing to their high theoretical energy density (~3500 Wh kg^{-1}) (*1*, *2*). However, their practical applications are hindered by their large overpotential (*3*), low rate capability (*4*), and poor cycling stability (*5*). The key to improving the performance of Li-O_2 batteries is to find effective cathode catalysts that increase the kinetics of the oxygen reduction reaction (ORR) and oxygen evolution reaction (OER) (*6*, *7*). Many cathode catalysts have been explored, including noble metals [Au (*8*), Ir (*9*), Ru (*10*), Pt (*11*), and Pd (*12*)], metal oxides [RuO_2 (*13*), MnO_2 (*14*), Co_3O_4 (*15*), and Ti_4O_7 (*16*)], perovskite oxides [$LaFeO_3$ (*17*), $LaNi_{1-x}Mg_xO_3$ (*18*), and $La_{0.75}Sr_{0.25}MnO_3$ (*19*)], single-atom catalysts (*20*), and carbon materials (*21*). Nevertheless, they often suffer from low catalytic activity/selectivity during cell discharging and charging (*22*). Moreover, the irregular precipitation of insoluble Li_2O_2 in the form of large toroid-like particles or thick films tends to block the active sites and inferior Li_2O_2/cathode contact, eventually leading to capacity decay during long-term cycling (*23*).

Metal-organic frameworks (MOFs) (*24*) and covalent organic frameworks (COFs) (*25*) have been explored as cathode catalysts to overcome the limitations of traditional cathode materials. MOFs and COFs are porous crystalline materials with high BET surface areas and tailorable functionalities, which allow the facile diffusion of O_2 and rational design of ORR/OER catalytic sites. Furthermore, uniform Li_2O_2 deposition can be realized by engineering the surface environment of MOFs and COFs. For example, MOF-based Li-O_2 batteries have shown promising discharge capacity and moderate charge kinetics owing to the uniformly dispersed metal catalytic sites (*26*–*29*). Unfortunately, the low chemical stability of coordination bonds in MOFs often leads to poor cyclability of MOF-based Li-O_2 batteries. COFs are built from robust covalent bonds, which are more compatible with the stability requirement of Li-O_2 batteries. However, COFs have not been applied in Li-O_2 batteries to our knowledge, possibly due to the lack of suitable metal sites for OER and ORR catalysis.

Metal-bis(dithiolene) and metalloporphyrin moieties are promising active sites for OER and ORR catalysis (*30*, *31*). Metal-bis(dithiolene) units have π-conjugated electronic structures and rich redox activity, which have been widely applied in the design of electrode materials (*32*). For example, MOFs with Ni-bis(dithiolene) moieties showed high conductivity (*33*) and bifunctional electrocatalytic activity toward the OER and ORR (*30*). On the other hand, M-N_4 centers in metalloporphyrins (*34*), metallophthalocyanines (*35*), and N-coordinated single-atom catalysts on carbon materials (*20*) were reported to accelerate the ORR/OER process and induce uniform Li_2O_2 deposition in Li-O_2 batteries. Therefore, we propose that efficient bifunctional ORR/OER catalysts can be realized by integrating Ni-bis(dithiolene) and Co-porphyrin units in a COF material. The bimetallic Ni/Co-COF will offer distinct advantages not only by increasing the concentration of active centers for ORR/OER catalysis but also by guiding uniform Li_2O_2 nucleation on periodically arranged Ni/Co sites.

In this work, a bimetallic COF was synthesized by the assembly of $Ni(bded)_2$ (bded = bis[1,2-di(4-formylphenyl)ethylene-1,2-ditholate]) and 5,10,15,20-tetrakis(4-aminophenyl)-porphinatocobalt. Meanwhile, the nonmetallic or single metallic isostructural COFs were also synthesized by replacing $Ni(bded)_2$ with its organic analog 2,3,6,7-tetra (4-formylphenyl)-tetrathiafulvalene (TTF-TBA) or using free-based porphyrin linkers 5,10,15,20-tetrakis (4-aminophenyl) porphinato. The combination of Ni-

[1]State Key Laboratory of Coordination Chemistry, Key Laboratory of Mesoscopic Chemistry of MOE, School of Chemistry and Chemical Engineering, Nanjing University, Nanjing 210023, P. R. China. [2]Center of Energy Storage Materials & Technology, College of Engineering and Applied Sciences, Jiangsu Key Laboratory of Artificial Functional Materials, National Laboratory of Solid State Microstructures, and Collaborative Innovation Center of Advanced Microstructures, Nanjing University, Nanjing 210023, P. R. China.
*Corresponding author. Email: zuojl@nju.edu.cn (J.-L.Z.); majing@nju.edu.cn (J.M.); pinghe@nju.edu.cn (P.H.)
†These authors contributed equally to this work.

bis(dithiolene) and Co-porphyrin resulted in a bimetallic Ni/Co-COF with a high BET surface area (116 $m^2 g^{-1}$), fairly good electrical conductivity (1.18×10^{-4} S m^{-1}), excellent chemical stability, and bifunctional ORR/OER activity as the Li-O_2 battery cathode. Li-O_2 batteries with Ni/Co-COF cathodes have low discharge/charge potential gap (1.0 V) and stable cycling for 200 cycles at a current density of 500 mA g^{-1}, which is much better than that of nonmetal or single metal–based isostructural COFs. Furthermore, the important role of Ni and Co centers in promoting the ORR/OER and inducing uniform Li_2O_2 deposition was supported by control experiments and density functional theory (DFT) calculations. This work will open up an avenue for designing advanced electrocatalysts for aprotic Li-O_2 batteries and beyond.

RESULTS AND DISCUSSION

Design and synthesis of bimetallic co/Ni-COF

Ni-bis(dithiolene) can be regarded as an inorganic analog of TTF (*32*). Therefore, the structures of TTF-COFs provide a blueprint for the design of bimetallic Co/Ni-COFs. For example, the Lan group has constructed a series of stable and highly crystalline metalloporphyrin-TTF–based COFs through the assembly of metallated 5,10,15,20-tetrakis (4-aminophenyl) porphinato (M-TAPP, M= Co, Ni, Cu, Zn, and Mn) and TTF-TBA (Fig. 1, A, B, D, and F) (*36*–*38*). Theoretically, replacing TTF-TBA with Ni(bded)$_2$ to connect with M-TAPP will lead to COFs that are isostructural to M-TTCOFs (Fig. 1, C, E, and G). As expected, the solvothermal reaction of Ni(bded)$_2$ with M-TAPP at 120°C gave rise to two isostructural COFs, namely, Ni-TAPP-2H and Ni-TAPP-Co.

Structure and characterization

The structure of Ni-TAPP-Co was confirmed by Pawley refinements against the powder x-ray diffraction (PXRD) pattern, while the structural simulation was performed by Materials Studio (Fig. 2A). For Ni-TAPP-Co, Pawley refinement based on the *P*1 space group gave lattice parameters of a = 31.70 Å, b = 20.47 Å, c = 5.17 Å, α = β = 70°, and γ = 90°. The diffraction peaks at 5.17°, 5.84°, 10.36°, 11.69°, and 21.77° were assigned to the ($1\bar{1}0$), (110), ($2\bar{2}0$), (220), and ($01\bar{1}$) facets, respectively. The simulated diffraction pattern of Ni-TAPP-Co matches well with the experimental data (*R*p = 1.21% and *R*wp = 1.52%). This structure of Ni-TAPP-Co shows a two-dimensional (2D) ***sql*** net with Ni-bis(dithiolene) and Co-porphyrin units alternately arranged in the layer. The layers adopt an eclipsed AA-stacking mode, forming 1D channels along

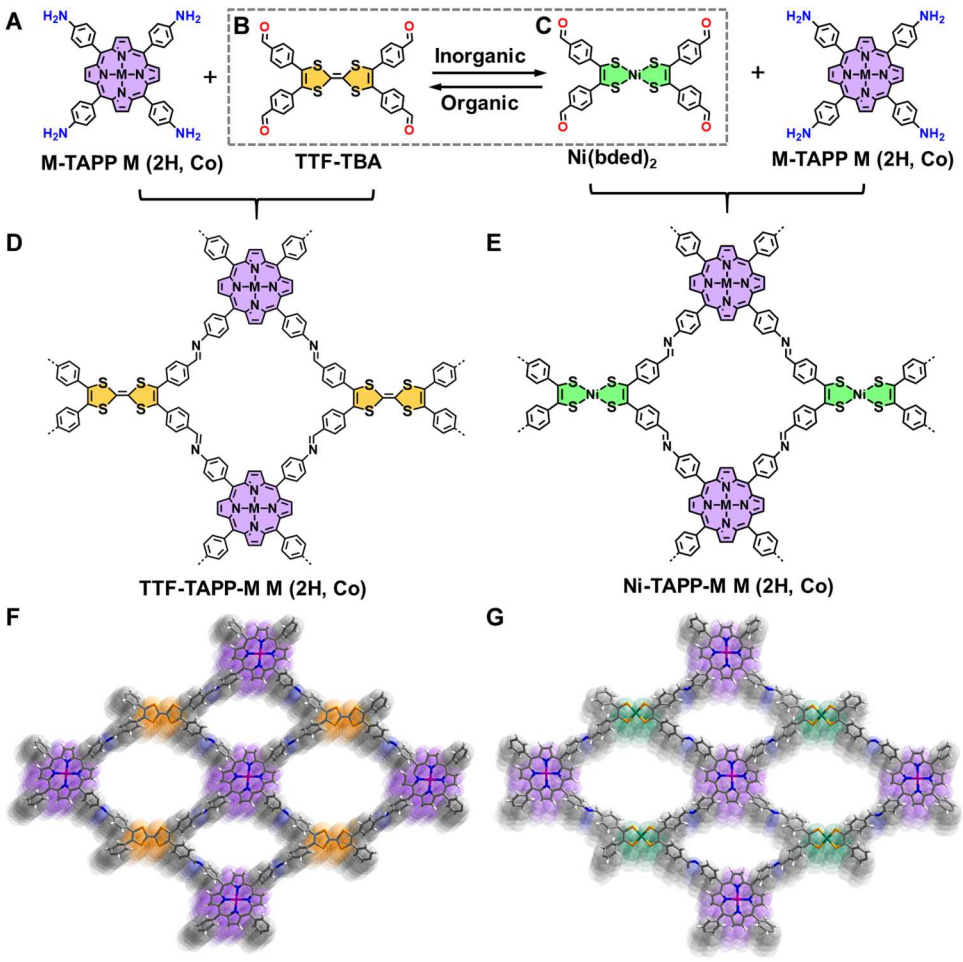

Fig. 1. Schematic representation for the design of COFs. (**A** to **C**) Molecular structures of M-TAPP (M = 2H, Co), TTF-TBA, and Ni(bded)$_2$. Molecular structures of COFs, denoted as TTF-TAPP-M (**D**) and Ni-TAPP-M (**E**). Extended structures of mesoporous 2D TTF-TAPP-M (**F**) and Ni-TAPP-M (**G**).

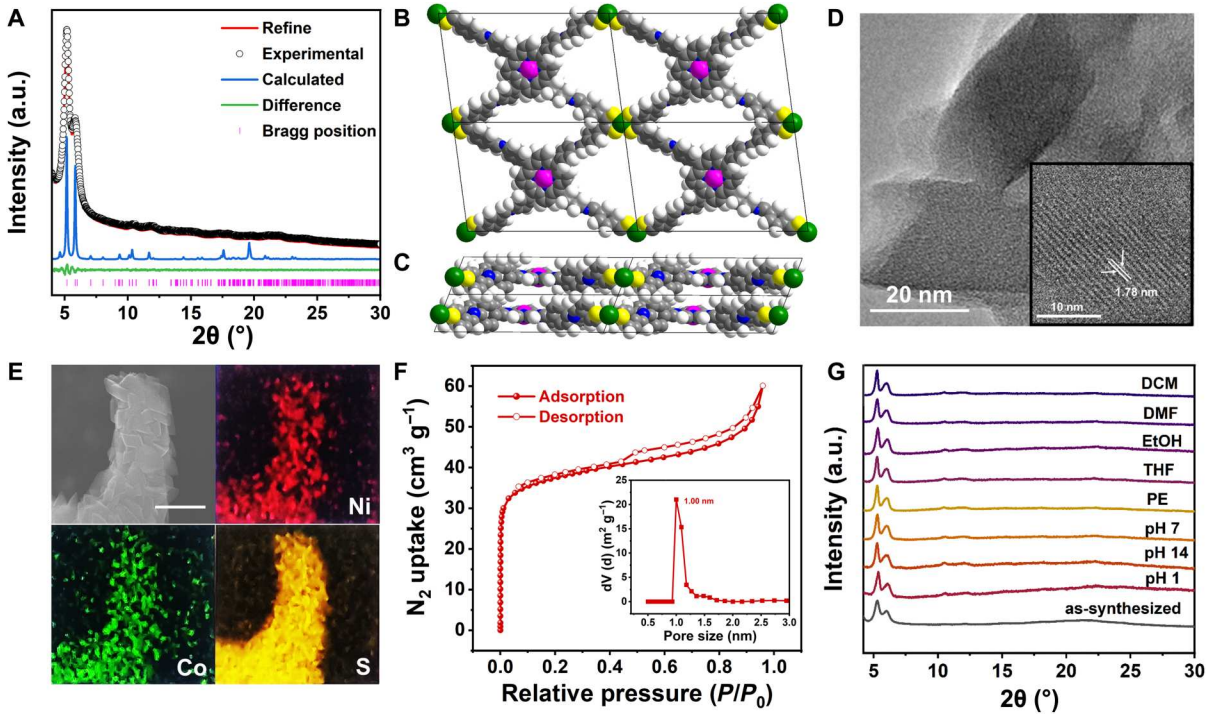

Fig. 2. Structural characterization of Ni-TAPP-Co. (**A**) Experimental (black dot) and simulated (red line) PXRD patterns of Ni-TAPP-Co. (**B**) Top and (**C**) side views of Ni-TAPP-Co. (**D**) HR-TEM image of Ni-TAPP-Co. (**E**) SEM and element mapping of Ni-TAPP-Co (scale bar, 500 nm). (**F**) N_2 adsorption-desorption isotherms of Ni-TAPP-Co (inset pore-size distribution profile). (**G**) PXRD patterns showing the stability of Ni-TAPP-Co.

the *c*-axis (Fig. 2, B and C). Notably, Ni-TAPP-Co is supported by both Ni-dithiolene coordination bonds (along the 100 direction) and imine covalent bonds (along the 110 and $1\bar{1}0$ directions), which represents a bridge between MOFs and COFs. TTF-TAPP-2H, TTF-TAPP-Co, and Ni-TAPP-2H are isostructural to Ni-TAPP-Co, as revealed by their similar PXRD patterns (figs. S1 to S3).

The structures of Ni-TAPP-2H and Ni-TAPP-Co were further supported by high-resolution transmission electron microscopy (HRTEM; Fig. 2D and fig. S4). Taking Ni-TAPP-Co as an example, the rectangular lattice and the 1D channels were clearly observed in the HRTEM images. The *d*-spacings of 1.78 nm correspond to the (010) crystal planes. In addition, Fourier transform infrared spectroscopy was conducted to confirm the successful synthesis of Ni-TAPP-2H and Ni-TAPP-Co (fig. S5). The formation of C═N bonds in Ni-TAPP-2H and Ni-TAPP-Co was indicated by the emergence of peaks at 1621 cm^{-1} accompanied by a decrease in the C═O (1701 cm^{-1}) stretching band of $Ni(bded)_2$ and the N─H (3200 to 3500 cm^{-1}) stretching bands. Ni-TAPP-2H and Ni-TAPP-Co show a broad absorption band with an edge at 1800 nm via ultraviolet-visible diffuse reflectance spectroscopy (fig. S6). Moreover, the optical energy gaps of Ni-TAPP-2H and Ni-TAPP-Co were estimated to be 0.73 and 0.75 eV by the Tauc plot, respectively (fig. S7). The morphology and elemental analysis of Ni-TAPP-Co and Ni-TAPP-2H were characterized by scanning electron microscopy (SEM) and energy-dispersive x-ray spectroscopy (EDS; Fig. 2E and fig. S8). The SEM image of Ni-TAPP-Co shows the aggregation of prism-shaped nanocrystals (~100 nm). EDS elemental mapping analysis further reveals that Ni, S, and Co are uniformly distributed in Ni-TAPP-Co particles. The elemental ratios of Ni, S, and Co for Ni-TAPP-Co estimated by inductively coupled plasma measurements are consistent with the theoretical values (table S1).

Porosity, stability, and conductivity measurements

The porosity and surface area of Ni-TAPP-Co and Ni-TAPP-2H were evaluated by N_2 adsorption measurements at 77 K (Fig. 2F and fig. S9). Both materials show a sharp uptake at a low pressure of ~0.05 P/P_0, which is a typical characteristic of microporous materials. The inclination of isotherms and slight hysteresis at ~0.8 P/P_0 is attributed to the mesopores and macropores from the packing of COF nanoparticles. The BET surface areas of Ni-TAPP-Co and Ni-TAPP-2H were estimated to be 116 and 168 $m^2\ g^{-1}$, respectively. The slightly lower BET surface area of Ni-TAPP-Co than Ni-TAPP-2H is related to the higher material density caused by Co atoms. The DFT pore size distribution analysis from the N_2 adsorption branch gives pore sizes of 1.00 nm for Ni-TAPP-Co and 1.18 nm for Ni-TAPP-2H, which are in good agreement with the structural models.

To investigate the chemical stability of Ni-TAPP-Co and Ni-TAPP-2H, two samples were exposed to different chemical environments for 24 hours, including dichloromethane, tetrahydrofuran (THF), ethanol (EtOH), *N*,*N*-dimethylformamide (DMF), petroleum ether (PE), water (pH 7), 0.1 M HCl (pH 1), and 1 M KOH (pH 14). Ni-TAPP-Co and Ni-TAPP-2H maintained their crystalline structure after the stability tests, as demonstrated by the unaltered PXRD peaks and the retained imine bond peaks in the infrared spectra (Fig. 2G and figs. S10 and S11). Thermogravimetric analysis reveals that both COFs have high thermal stability up to 350°C in air (fig. S12). Using a two-point measurement at 298 K,

the average electrical conductivity values of the pressed pellets were determined to be 2.07×10^{-5}, 9.34×10^{-5}, 8.46×10^{-6}, and 1.18×10^{-4} S m^{-1} for TTF-TAPP-2H, TTF-TAPP-Co, Ni-TAPP-2H, and Ni-TAPP-Co, respectively (fig. S13 and table S2). The high electrical conductivity of TTF-TAPP-M and Ni-TAPP-M can be attributed to the conducting pathways formed by S···S interactions between π-stacked TTF moieties and Ni-bis(dithiolene) moieties. In addition, the electron hopping between adjacent porphyrin units may also contribute to the conductivity, where the Co center in the porphyrin has been known to facilitate the electron transfer (*39*). Notably, the bimetallic Ni-TAPP-Co exhibit the highest conductivity, which can be attributed to the existence of both S···S electron transfer chains and Co-centered electron hopping pathways highlighting the advantage of bimetallic COFs. The high porosity, chemical stability, and electrical conductivity promised Ni-TAPP-Co to be a suitable cathode material for Li-O_2 batteries.

Li-O_2 cell performance

To evaluate the electrocatalytic property of the Ni-TAPP-Co cathode, particularly the bifunctional ORR and OER catalytic activity, aprotic Li-O_2 batteries were assembled. In addition, nonmetallic or single metallic COFs (TTF-TAPP-2H, TTF-TAPP-Co, and Ni-TAPP-2H) were used as control groups (Fig. 3, A to D). Li-O_2 batteries with Ni-TAPP-Co and other control cathodes are tested under the galvanostatic mode with a discharge/charge capacity of 1000 mAh g^{-1} at a constant current density of 200 mA g^{-1}. As shown in Fig. 3E, the discharge terminal voltage of TTF-TAPP-2H rapidly dropped to 1.5 V with a high charging potential of ~4.5 V after 60 charge/discharge cycles, demonstrating the poor ORR/OER catalytic performance of the nonmetallic COF-based cathode. Specifically, the TTF-TAPP-Co–based Li-O_2 battery showed decreased charging potential (4.0 V), although the discharging potential dropped to 2.3 V after 40 cycles (Fig. 3F). This result indicates that Co-porphyrin centers in TTF-TAPP-Co effectively accelerated the OER process during charging. The Ni-TAPP-2H–based Li-O_2 battery shows a similar charging potential (4.0 V) similar to that of TTF-TAPP-Co, suggesting that Co and Ni sites are both active for OER. On the other hand, Ni-TAPP-2H exhibits stable discharging profiles (2.75 V after 60 cycles), which were tentatively attributed to the enhanced ORR kinetics and more uniform Li_2O_2 deposition on Ni sites (Fig. 3G). Notably, the Ni-TAPP-Co cathode with bimetallic active sites (Co and Ni) provides a remarkably low overpotential and outstanding cyclic stability compared to monometallic materials (Fig. 3H). The first-cycle discharge-charge curves are compared in fig. S14. The Ni-TAPP-Co cathode shows the lowest discharge/charge potential gap (0.61 V) and highest round-trip efficiency (78.5%) compared to TTF-TAPP-Co (0.72 V, 72.1%), Ni-TAPP-2H (0.81 V, 73.5%), and TTF-TAPP-2H (1.25 V, 64.1%), respectively. In addition, monomer-based cathodes [TTF-TBA, Ni(bded)$_2$, 2H-TAPP, and Co-TAPP], following the same way as COF-cathodes, assembled the corresponding Li-O_2 batteries. However, the discharge terminal voltages of monomer [TTF-TBA, Ni(bded)$_2$, 2H-TAPP, and Co-TAPP] rapidly dropped, and the high charging potential after 10 charge/discharge cycles demonstrates the poor ORR/OER catalytic performance and the low stability of the monomer-based cathode (fig. S15). The impressive electrochemical performances of Ni/Co COF-based catalysts are attributed to their uniform porosity, high surface areas, and enhanced chemical stability.

The ORR/OER activities of TTF-TAPP-2H, TTF-TAPP-Co, Ni-TAPP-2H, and Ni-TAPP-Co were further evaluated by cyclic voltammetry (CV) profiles at a scan rate of 0.1 mV s^{-1} (fig. S16). The Ni-TAPP-Co cathode displays a higher ORR onset potential (~2.90 V), lower OER potential (~3.2 V), and larger redox peak areas, demonstrating its superior ORR/OER activity and high specific capacity in Li-O_2 batteries. In addition, electrochemical impedance spectroscopy (EIS) was conducted before and after cycling tests, and the corresponding equivalent circuit is shown in fig. S17, where R_s, CPE, R_{ct}, and W_o represent the solution resistance, double-layer capacitance, charge-transfer resistance, and Warburg impedance, respectively. The fitted R_{ct} of Ni-TAPP-Co cathode exhibits a minimal increase from 22.2 to 33.6 ohms, while TTF-TAPP-2H (from 46.5 to 150.9 ohms), TTF-TAPP-Co (from 26.6 to 55.3 ohms), and Ni-TAPP-2H (from 28.2 to 58.5 ohms) show a pronounced increase in impedance (R_{ct}). This is consistent with the stable discharging-charging profile of the Ni-TAPP-Co cathode, signifying the important role of both Ni and Co centers in accelerating the ORR/OER kinetics and inducing uniform Li_2O_2 deposition.

The rate performance of Li-O_2 from 200 to 500 mA g^{-1} under a limited capacity (1000 mAh g^{-1}) was further evaluated (Fig. 3I and fig. S18). The Ni-TAPP-Co cathode exhibits the highest discharge potential (2.80, 2.78, and 2.75 V) and the smallest voltage gaps of 0.61, 0.75, and 0.92 V at 200, 300, and 500 mA g^{-1}, respectively. The deep discharge-charge process of the four Li-O_2 batteries was measured in the range of 2.0 to 4.5 V under 500 mA g^{-1}. The Ni-TAPP-Co cathode exhibits the largest discharge capacity of 17,104 mAh g^{-1}, which is higher than those of Ni-TAPP-2H (7519 mAh g^{-1}), TTF-TAPP-Co (4213 mAh g^{-1}), and TTF-TAPP-2H (2786 mAh g^{-1}; Fig. 3J). The Ni-TAPP-Co cathode delivers a much lower discharge/charge potential gap (1.38 V) than Ni-TAPP-2H (1.75 V), TTF-TAPP-Co (1.95 V), and TTF-TAPP-2H (2.10 V), suggesting faster Li_2O_2 decomposition kinetics and higher reversibility of the Ni-TAPP-Co cathode. Moreover, the cycling performances of the four cathodes were compared with a constant capacity of 1000 mAh g^{-1} at a large current density of 500 mA g^{-1}. The Ni-TAPP-Co cathode shows high cycling stability with minimal change in charging/discharging voltage after 200 cycles (Fig. 3K). For comparison, the TTF-TAPP-2H, TTF-TAPP-Co, and Ni-TAPP-2H cathodes degraded quickly after 13, 57, and 120 cycles (fig. S19). The performance of the Ni-TAPP-Co cathode is higher than most nonprecious metal–based cathode materials in the literature and even comparable to noble metal–based catalysts (Fig. 3L and table S3).

The compositional change of Ni-TAPP-Co cathodes during the 20th charging/discharging cycle (2000 mAh g^{-1}, 200 mA g^{-1}) was studied by PXRD, XPS, Raman spectroscopy, and SEM. As shown in Fig. 4A, the peak at 5.17° was attributed to the $(1\bar{1}0)$ diffraction of Ni-TAPP-Co, while the strong background peaks at 17.5° and 26.2° were assigned to carbon paper. After discharging, the emerging peaks at 23.3°, 33.8°, 35.2°, and 41.2° correspond to the (200), (201), (110), and (111) diffraction peaks of Li_2O_2 (marked as *). Raman spectra of discharged cathodes show a new peak at 793 cm^{-1}, which disappears after recharging, corresponding to the formation and decomposition of Li_2O_2 (Fig. 4B). In contrast, the discharged and recharged TTF-TAPP-2H electrode shows an obvious Li_2CO_3 peak (fig. S20). This is attributed to the decomposition of the electrolyte at high charging voltage, which ultimately induces

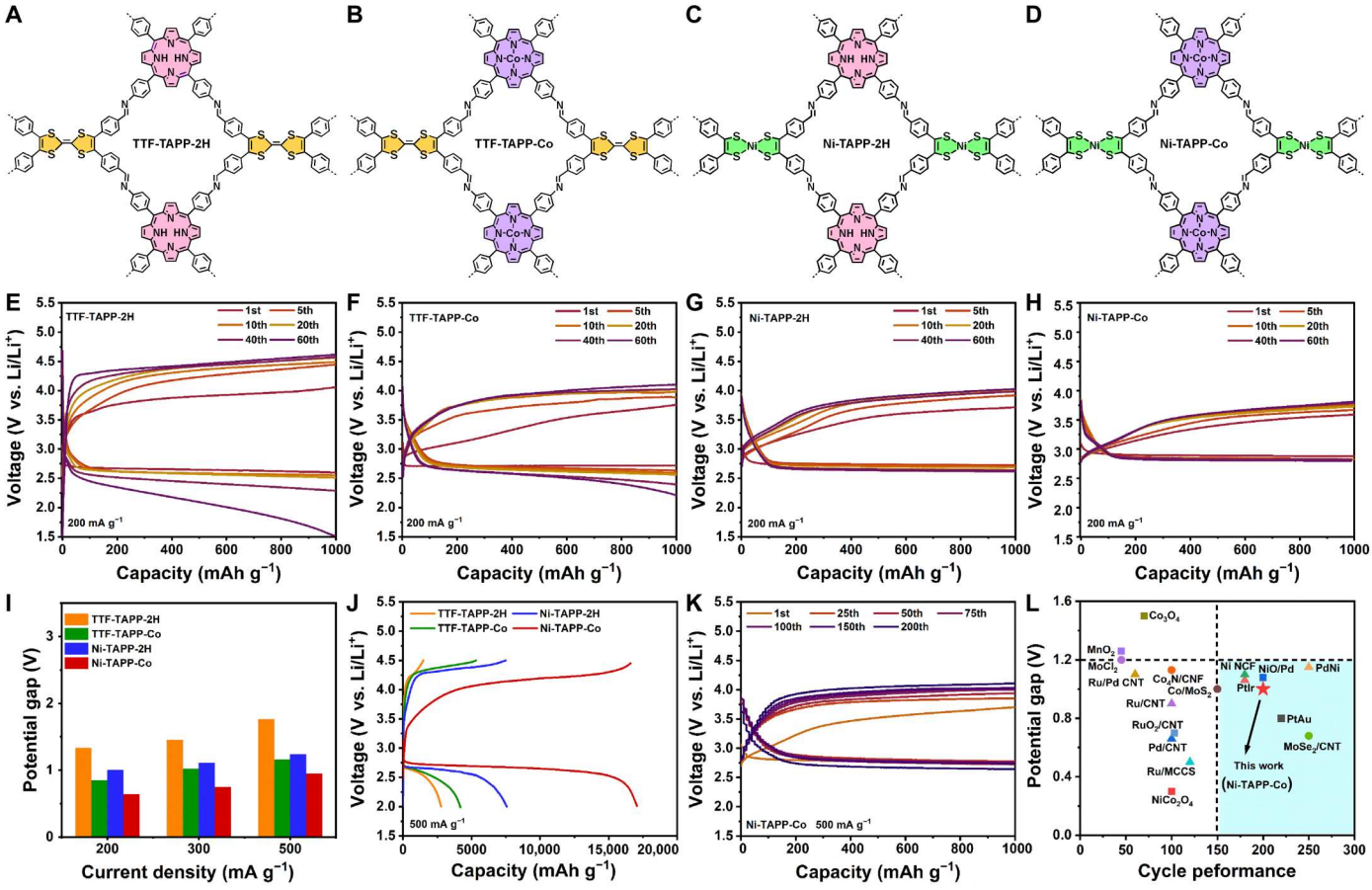

Fig. 3. Electrochemical performance of Li-O_2 batteries using different COF cathode catalysts. (**A** to **D**) Molecular structures of TTF-TAPP-2H, TTF-TAPP-Co, Ni-TAPP-2H, and Ni-TAPP-Co. Charging/discharging curves of the COF cathodes with a limited capacity of 1000 mAh g^{-1} at 200 mA g^{-1}, (**E**) TTF-TAPP-2H, (**F**) TTF-TAPP-Co, (**G**) Ni-TAPP-2H, and (**H**) Ni-TAPP-Co. (**I**) Discharge/charge potential gap of different COF cathode catalysts under current densities of 200, 300, and 500 mA g^{-1}. (**J**) The galvanostatic profiles for the four cathodes under full discharging and charging conditions at 500 mA g^{-1} (2.0 to 4.5 V versus Li/Li^+). (**K**) Long-term cycling performance of the Ni-TAPP-Co cathode catalyst at a current density of 500 mA g^{-1}. (**L**) Comparison of cyclic life and discharge/charge potential gap between the Ni-TAPP-Co cathode catalyst and other solid catalysts in previous reports.

the formation of Li_2CO_3 via side reactions. Meanwhile, the Ni-TAPP-Co lattice diffractions are maintained after charging/discharging, confirming the stability of Ni-TAPP-Co. [NiS_4] units in Ni-TAPP-2H and Ni-TAPP-Co undergo reversible redox processes during discharge/charge as confirmed by XPS (fig. S21).

In situ differential electrochemical mass spectrometry (DEMS) was further conducted to monitor the gas evolution of the Li-O_2 batteries during the charging process (Fig. 4C and fig. S22). Only O_2 was detected from the Ni-TAPP-Co cathode with a charge-to-mass ratio of 1.95e^-/O_2, which is close to the theoretical value of 2e^-/O_2 based on the reversible reaction: $2Li^+ + O_2 + 2e^- \leftrightarrow Li_2O_2$. The nonmetallic TTF-TAPP-2H cathode releases CO_2 during charging, which is attributed to the decomposition of the by-product Li_2CO_3 and the electrolyte at high charging potential (*40*, *41*). Therefore, the Ni-TAPP-Co catalyst not only enhanced the formation and decomposition of Li_2O_2 but also suppressed the side reaction during charging/discharging.

To investigate the effect of Co and Ni centers on the morphology of Li_2O_2 on the cathode surface, TTF-TAPP-2H, Ni-TAPP-2H, TTF-TAPP-Co, and Ni-TAPP-Co cathodes were analyzed by SEM after discharging (2000 mAh g^{-1}, 200 mA g^{-1}). TTF-TAPP-2H, Ni-TAPP-2H, TTF-TAPP-Co, and Ni-TAPP-Co cathodes exhibit three types of morphologies after a full discharge process. Li_2O_2 on the TTF-TAPP-2H cathode exhibits large toroid-shaped particles (Fig. 4D), while compact film-like Li_2O_2 is formed on the Ni-TAPP-2H and TTF-TAPP-Co cathodes (Fig. 4, E and F). These morphologies of Li_2O_2 have been commonly observed in the literature. On the basis of the literature (*42*–*45*), the morphology of Li_2O_2 is controlled by the adsorption energy of $*LiO_2$ species on the surface. The toroid-like discharged product may follow the solution-mediated growing model due to the weak $*LiO_2$ binding and low affinity with Li_2O_2. On the other hand, the thick films of Li_2O_2 obey the surface-dominated growing model. Li_2O_2 formed wrinkled nanosheets on the surface of the Ni-TAPP-Co cathode, which is markedly different from the toroidal particles or films (Fig. 4G). The nanosheet morphology can be related to the high concentration of Co and Ni sites on Ni-TAPP-Co as $*LiO_2$ binding sites to induce fast Li_2O_2 nucleation. This observation is in accordance with the literature on the morphology of Li_2O_2 growing on different cathodes (*46*–*48*). Compared with traditional toroidal particles or thick films, wrinkled nanosheets of Li_2O_2 have higher surface areas and better

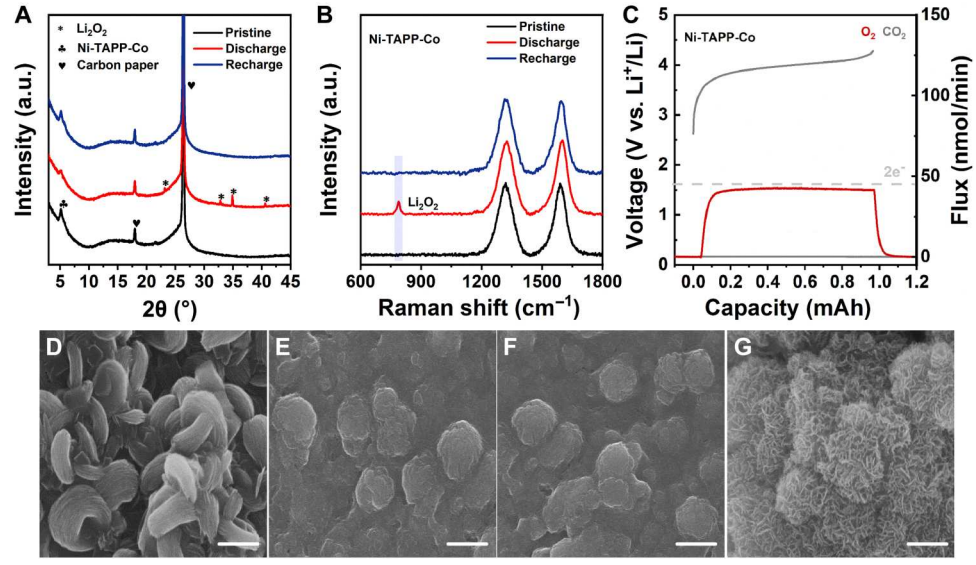

Fig. 4. Product characterizations of battery reactions. (**A**) XRD patterns and (**B**) Raman of Ni-TAPP-Co cathode catalysts at different stages (Pristine, Discharge, and Recharge). (**C**) DEMS test during charging of the Li-O_2 battery with the Ni-TAPP-Co cathode catalyst. SEM images (scale bars, 500 nm) of discharged TTF-TAPP-2H (**D**), TTF-TAPP-Co (**E**), Ni-TAPP-2H (**F**), and Ni-TAPP-Co (**G**).

Li_2O_2/Ni-TAPP-Co interfaces, which enhance electron transportation for predominant recovery capability (fig. S23).

Effect of bimetallic COF on ORR/OER catalysis and Li_2O_2 deposition

The bifunctional of the Ni-TAPP-Co cathode during the ORR/OER process is rationalized by DFT calculations. The elementary steps of Li_2O_2 formation on Ni-TAPP-2H (Ni sites), TTF-TAPP-Co (Co sites), and Ni-TAPP-Co (Ni sites, Co sites) are exothermal reactions at an open circuit voltage (U = 0 V), manifesting a spontaneous discharge process (Fig. 5, A to D, and fig. S24). In monometallic COFs, the binding free energy (ΔG_{ads}) of $*LiO_2$ on the Ni site (−2.02 eV for Ni-TAPP-2H) is slightly lower than that of the Co site (−1.98 eV for TTF-TAPP-Co), suggesting a higher ORR activity of Ni-bis(dithiolene) than Co-porphyrin. In addition, the $*LiO_2$ binding free energy on Ni (−2.05 eV) and Co sites (−2.01 eV) in bimetallic Ni-TAPP-Co is comparable to those of Ni-TAPP-2H and TTF-TAPP-Co. The slightly different $*LiO_2$ binding free energy of Co sites in monometallic and bimetallic COFs is tentatively attributed to the electron-withdrawing effect of Ni-bis(dithiolene) ligands covalently linked to the Ni centers, which reduced the electron density on Ni centers and enhanced the $*LiO_2$ binding. A similar argument can be made to explain the slightly lower $*LiO_2$ binding free energy of Ni sites in Ni-TAPP-Co than in Ni-TAPP-2H. However, the electronic interaction between Co and Ni centers is not pronounced considering their long distances (1.8 nm). Therefore, the coexisting Ni (ΔG_{ads} = −2.05 eV) and Co sites (ΔG_{ads} = −2.01 eV) in Ni-TAPP-Co cathode acts as $*LiO_2$ binding sites to induce the nucleation and formation of Li_2O_2 nanosheets, which is in agreement with the SEM experiment. The energy paths remain downhill until the applied voltages reach 2.03, 1.78, 2.02, and 1.68 V for Ni-TAPP-Co (Ni sites, U_{DC} = 2.03 V), Ni-TAPP-Co (Co sites, U_{DC} = 1.78 V), Ni-TAPP-2H (Ni sites, U_{DC} = 2.02 V), and TTF-TAPP-Co (Co sites, U_{DC} = 1.68 V), respectively. Subsequently, the calculated OER overpotential of Ni-TAPP-Co (Ni sites: 0.74 V, Co sites: 1.23 V) is lower than that of TTF-TAPP-Co (Co sites: 1.32 V), which is in line with the results in Fig. 3 (F to H). However, the OER/ORR process of the active Ni sites is comparable in Ni-TAPP-Co and Ni-TAPP-2H. Therefore, the higher performance of the Ni-TAPP-Co cathode is mainly attributed to the morphology control of Li_2O_2 nanosheets by Ni/Co sites during discharge and charge. Inspired by the experimental and theoretical calculation results, plausible routes are proposed to elaborate the formation and decomposition process of Li_2O_2 on the above cathodes, as illustrated in Fig. 5 (E to H).

In summary, a bimetallic COF with Ni-bis(dithiolene) and Co-porphyrin centers has been synthesized as a bifunctional ORR/OER catalyst for Li-O_2 batteries. The combination of Ni-bis(dithiolene) and Co-porphyrin in a porous COF has led to a material with high porosity, excellent stability, good conductivity, and electrocatalytic activity toward the aprotic ORR/OER. The Li-O_2 battery with the Ni-TAPP-Co cathode shows a low discharge/charge potential gap (1.0 V) and stable cycling performance (200 cycles). In situ and ex situ experiments along with DFT calculations reveal the important role of Co and Ni sites in catalyzing the ORR/OER and inducing uniform Li_2O_2 deposition. These results highlight the great promise of bimetallic COFs in the rational design of efficient cathode materials for Li-O_2 batteries. Considering the unlimited structural tunability and precisely controllable active sites of COFs, advanced cathode materials can be expected to realize efficient and stable Li-O_2 batteries.

MATERIALS AND METHODS

Synthesis of Ni-TAPP-2H

A Pyrex tube (18 × 9 mm outer diameter × inner diameter) was charged with 2H-TAPP (0.02 mmol, 13.5 mg), $Ni(bded)_2$ (0.02 mmol, 13.1 mg), 1,4-dioxane (0.75 ml), mesitylene (0.25 ml), and aqueous acetic acid (6 M, 0.2 ml), and the mixture was sonicated for 15 min. After three freeze-pump-thaw cycles, the Pyrex tube was sealed under vacuum and heated at 120°C for 72 hours. The

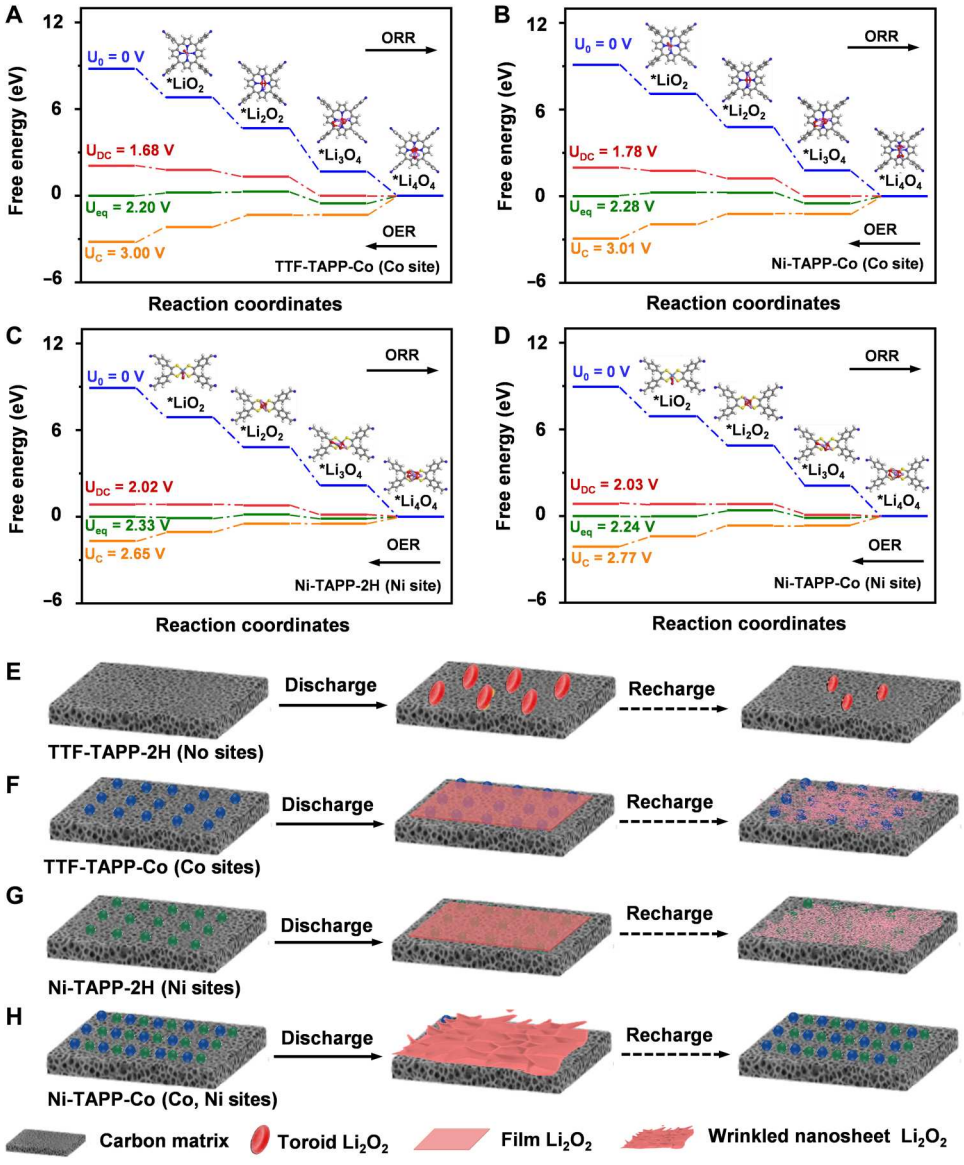

Fig. 5. DFT calculations and schematic illustration of the reaction pathway. Free energy diagrams of battery reactions on the surface of the (**A**) Co site in TTF-TAPP-Co, (**B**) Co site in Ni-TAPP-Co, (**C**) Ni site in Ni-TAPP-2H, and (**D**) Ni site in Ni-TAPP-Co. Schematic illustrations of the discharge-charge processes for the TTF-TAPP-2H (**E**), TTF-TAPP-Co (**F**), Ni-TAPP-2H (**G**), and Ni-TAPP-Co (**H**) cathodes.

dark purple precipitate was isolated by filtration and washed with CH_3OH and THF. The dark solid was further washed with THF via Soxhlet extraction for 24 hours. Last, the product was dried at 100°C under vacuum for 24 hours to obtain the activated sample.

Synthesis of Ni-TAPP-co

The synthesis of Ni-TAPP-Co is similar to that of Ni-TAPP-2H except that Co-TAPP (0.02 mmol, 14.7 mg) was used instead of 2H-TAPP.

Electrochemical measurements

The electrochemical performance of Li-O_2 batteries was tested following the literature (*49*, *50*) by 2032 coin-type cells with holes on the cathode side. The battery consists of a lithium metal anode (Φ 12 mm), a glass microfiber separator (Whatman, Φ 14 mm), 0.2 ml of electrolyte (1 M LiTFSI in TEGDME), and a preobtained cathode (Φ 12 mm). All batteries were assembled in an argon-filled glovebox with a pressure of 1 atm (O_2 and H_2O levels <0.1 ppm) and were lastly placed in a homemade battery testing device. All the battery testing devices should be aerated with pure O_2 for 20 min and then left to rest for 6 hours before testing. We used a LAND cycler (CT2001A) and an electrochemical workstation (CHI740E; Shanghai Chenhua) to perform the electrochemical measurements. The CV curves were measured with a voltage range of 2.0 to 4.5 V and a scan rate of 10 mV s^{-1} by an electrochemical station. The EIS Nyquist plots were measured with a frequency range of 100 kHz to 0.1 Hz by an electrochemical station. Raman spectroscopy was carried out on aRenishaw inVia confocal Raman microscope with

the excitation light of an air-cooled He-Ne laser at 633 nm through a 50× long working distance lens (Leica Microsystems Inc.). The DEMS result was collected by a homemade Li-O_2 battery mold with two poly(ether-ether-ketone) (PEEK) valves connected to a quadrupole mass spectrometer with a turbomolecular pump (Pfeiffer Vacuum). The remaining gas was purged to the mass spectrometer chamber (PrismaPro QMG 250 M2).

Supplementary Materials

This PDF file includes:

Supplementary Text
Figs. S1 to S27
Tables S1 to S5
References

REFERENCES AND NOTES

1. P. Zhang, Y. Zhao, X. Zhang, Functional and stability orientation synthesis of materials and structures in aprotic Li–O_2 batteries. *Chem. Soc. Rev.* **47**, 2921–3004 (2018).
2. P. G. Bruce, S. A. Freunberger, L. J. Hardwick, J.-M. Tarascon, Li–O_2 and Li–S batteries with high energy storage. *Nat. Mater.* **11**, 19–29 (2012).
3. J. Lu, Y. Lei, K. C. Lau, X. Luo, P. du, J. Wen, R. S. Assary, U. das, D. J. Miller, J. W. Elam, H. M. Albishri, D. A. El-Hady, Y.-K. Sun, L. A. Curtiss, K. Amine, A nanostructured cathode architecture for low charge overpotential in lithium-oxygen batteries. *Nat. Commun.* **4**, 2383 (2013).
4. C. Xia, C. Y. Kwok, L. F. Nazar, A high-energy-density lithium-oxygen battery based on a reversible four-electron conversion to lithium oxide. *Science* **361**, 777–781 (2018).
5. L. Majidi, P. Yasaei, R. E. Warburton, S. Fuladi, J. Cavin, X. Hu, Z. Hemmat, S. B. Cho, P. Abbasi, M. Vörös, L. Cheng, B. Sayahpour, I. L. Bolotin, P. Zapol, J. Greeley, R. F. Klie, R. Mishra, F. Khalili-Araghi, L. A. Curtiss, A. Salehi-Khojin, New class of electrocatalysts based on 2D transition metal dichalcogenides in ionic liquid. *Adv. Mater.* **31**, 1804453 (2019).
6. N. B. Aetukuri, B. D. McCloskey, J. M. García, L. E. Krupp, V. Viswanathan, A. C. Luntz, Solvating additives drive solution-mediated electrochemistry and enhance toroid growth in non-aqueous Li–O_2 batteries. *Nat. Chem.* **7**, 50–56 (2015).
7. C. Zheng, W. Ding, C. Wang, N-methyl-N-propyl pyrrolidine bromide (MPPBr) as a bifunctional redox mediator for rechargeable Li–O_2 batteries. *J. Mater. Chem. A* **7**, 6180–6186 (2019).
8. Z. Peng, S. A. Freunberger, Y. Chen, P. G. Bruce, A reversible and higher-rate Li-O_2 battery. *Science* **337**, 563–566 (2012).
9. J. Lu, Y. J. Lee, X. Luo, K. C. Lau, M. Asadi, H.-H. Wang, S. Brombosz, J. Wen, D. Zhai, Z. Chen, D. J. Miller, Y. S. Jeong, J.-B. Park, Z. Z. Fang, B. Kumar, A. Salehi-Khojin, Y.-K. Sun, L. A. Curtiss, K. Amine, A lithium–oxygen battery based on lithium superoxide. *Nature* **529**, 377–382 (2016).
10. K. Liao, T. Zhang, Y. Wang, F. Li, Z. Jian, H. Yu, H. Zhou, Nanoporous Ru as a carbon- and binder-free cathode for Li–O_2 batteries. *ChemSusChem* **8**, 1429–1434 (2015).
11. Y.-C. Lu, H. A. Gasteiger, M. C. Parent, V. Chiloyan, Y. Shao-Horn, The influence of catalysts on discharge and charge voltages of rechargeable Li–oxygen batteries. *Electrochem. Solid-State Lett.* **13**, A69 (2010).
12. Y.-C. Lu, H. A. Gasteiger, Y. Shao-Horn, Catalytic activity trends of oxygen reduction reaction for nonaqueous Li-air batteries. *J. Am. Chem. Soc.* **133**, 19048–19051 (2011).
13. K. Liao, X. Wang, Y. Sun, D. Tang, M. Han, P. He, X. Jiang, T. Zhang, H. Zhou, An oxygen cathode with stable full discharge–charge capability based on 2D conducting oxide. *Energ. Environ. Sci.* **8**, 1992–1997 (2015).
14. A. Débart, A. J. Paterson, J. Bao, P. G. Bruce, α-MnO_2 nanowires: A catalyst for the O_2 electrode in rechargeable lithium batteries. *Angew. Chem. Int. Ed.* **47**, 4521–4524 (2008).
15. Y. Cui, Z. Wen, Y. Liu, A free-standing-type design for cathodes of rechargeable Li–O_2 batteries. *Energ. Environ. Sci.* **4**, 4727–4734 (2011).
16. S. Lee, G.-H. Lee, J.-C. Kim, D.-W. Kim, Magnéli-phase Ti_4O_7 nanosphere electrocatalyst support for carbon-free oxygen electrodes in lithium–oxygen batteries. *ACS Catal.* **8**, 2601–2610 (2018).
17. J.-J. Xu, Z.-L. Wang, D. Xu, F.-Z. Meng, X.-B. Zhang, 3D ordered macroporous $LaFeO_3$ as efficient electrocatalyst for Li–O_2 batteries with enhanced rate capability and cyclic performance. *Energ. Environ. Sci.* **7**, 2213–2219 (2014).
18. Z. Du, P. Yang, L. Wang, Y. Lu, J. B. Goodenough, J. Zhang, D. Zhang, Electrocatalytic performances of $LaNi_{1-x}Mg_xO3$ perovskite oxides as bi-functional catalysts for lithium air batteries. *J. Power Sources* **265**, 91–96 (2014).
19. J.-J. Xu, D. Xu, Z.-L. Wang, H.-G. Wang, L.-L. Zhang, X.-B. Zhang, Synthesis of perovskite-based porous $La_{0.75}Sr_{0.25}MnO_3$ nanotubes as a highly efficient electrocatalyst for rechargeable lithium–oxygen batteries. *Angew. Chem. Int. Ed.* **52**, 3887–3890 (2013).
20. P. Wang, Y. Ren, R. Wang, P. Zhang, M. Ding, C. Li, D. Zhao, Z. Qian, Z. Zhang, L. Zhang, L. Yin, Atomically dispersed cobalt catalyst anchored on nitrogen-doped carbon nanosheets for lithium-oxygen batteries. *Nat. Commun.* **11**, 1576 (2020).
21. D. Zhai, H.-H. Wang, J. Yang, K. C. Lau, K. Li, K. Amine, L. A. Curtiss, Disproportionation in Li–O_2 batteries based on a large surface area carbon cathode. *J. Am. Chem. Soc.* **135**, 15364–15372 (2013).
22. Y. Shao, S. Park, J. Xiao, J.-G. Zhang, Y. Wang, J. Liu, Electrocatalysts for nonaqueous lithium–air batteries: Status, challenges, and perspective. *ACS Catal.* **2**, 844–857 (2012).
23. H.-D. Lim, B. Lee, Y. Zheng, J. Hong, J. Kim, H. Gwon, Y. Ko, M. Lee, K. Cho, K. Kang, Rational design of redox mediators for advanced Li–O_2 batteries. *Nat. Energy* **1**, 16066 (2016).
24. H. Li, M. Eddaoudi, M. O'Keeffe, O. M. Yaghi, Design and synthesis of an exceptionally stable and highly porous metal-organic framework. *Nature* **402**, 276–279 (1999).
25. A. P. Côté, A. I. Benin, N. W. Ockwig, M. O'Keffee, A. J. Matzger, O. M. Yaghi, Porous, crystalline, covalent organic frameworks. *Science* **310**, 1166–1170 (2005).
26. D. Wu, Z. Guo, X. Yin, Q. Pang, B. Tu, L. Zhang, Y.-G. Wang, Q. Li, Metal–organic frameworks as cathode materials for Li–O_2 batteries. *Adv. Mater.* **26**, 3258–3262 (2014).
27. Q. Li, P. Xu, W. Gao, S. Ma, G. Zhang, R. Cao, J. Cho, H.-L. Wang, G. Wu, Graphene/graphene-tube nanocomposites templated from cage-containing metal-organic frameworks for oxygen reduction in Li-O_2 batteries. *Adv. Mater.* **26**, 1378–1386 (2014).
28. Z. Liang, C. Qu, W. Guo, R. Zou, Q. Xu, Pristine metal–organic frameworks and their composites for energy storage and conversion. *Adv. Mater.* **30**, 1702891 (2018).
29. W. H. Choi, B. C. Moon, D. G. Park, J. W. Choi, K.-H. Kim, J.-S. Shin, M. G. Kim, K. M. Choi, J. K. Kang, Autogenous production and stabilization of highly loaded sub-nanometric particles within multishell hollow metal–organic frameworks and their utilization for high performance in Li–O_2 batteries. *Adv. Sci.* **7**, 2000283 (2020).
30. L. Lin, Q. Zhang, Y. Ni, L. Shang, X. Zhang, Z. Yan, Q. Zhao, J. Chen, Rational design and synthesis of two-dimensional conjugated metal-organic polymers for electrocatalysis applications. *Chem* **8**, 1822–1854 (2022).
31. H. Zhang, M. Zhu, O. G. Schmidt, S. Chen, K. Zhang, Covalent organic frameworks for efficient energy electrocatalysis: Rational design and progress. *Adv. Energy Sustainability Res.* **2**, 2000090 (2021).
32. S.-W. Ke, Y. Wang, J. Su, K. Liao, S. Lv, X. Song, T. Ma, S. Yuan, Z. Jin, J.-L. Zuo, Redox-active covalent organic frameworks with nickel–Bis(dithiolene) units as guiding layers for high-performance lithium metal batteries. *J. Am. Chem. Soc.* **144**, 8267–8277 (2022).
33. T. Kambe, R. Sakamoto, K. Hoshiko, K. Takada, M. Miyachi, J. H. Ryu, S. Sasaki, J. Kim, K. Nakazato, M. Takata, H. Nishihara, π-Conjugated nickel bis(dithiolene) complex nanosheet. *J. Am. Chem. Soc.* **135**, 2462–2465 (2013).
34. W. Zhang, W. Lai, R. Cao, Energy-related small molecule activation reactions: Oxygen reduction and hydrogen and oxygen evolution reactions catalyzed by porphyrin- and corrole-based systems. *Chem. Rev.* **117**, 3717–3797 (2017).
35. D. Sun, Y. Shen, W. Zhang, L. Yu, Z. Yi, W. Yin, D. Wang, Y. Huang, J. Wang, D. Wang, J. B. Goodenough, A solution-phase bifunctional catalyst for lithium–oxygen batteries. *J. Am. Chem. Soc.* **136**, 8941–8946 (2014).
36. M. Lu, J. Liu, Q. Li, M. Zhang, M. Liu, J. L. Wang, D.-Q. Yuan, Y.-Q. Lan, Rational design of crystalline covalent organic frameworks for efficient CO_2 photoreduction with H_2O. *Angew. Chem. Int. Ed.* **58**, 12392–12397 (2019).
37. H.-J. Zhu, M. Lu, Y.-R. Wang, S.-J. Yao, M. Zhang, Y.-H. Kan, J. Liu, Y. Chen, S.-L. Li, Y.-Q. Lan, Efficient electron transmission in covalent organic framework nanosheets for highly active electrocatalytic carbon dioxide reduction. *Nat. Commun.* **11**, 497 (2020).
38. Y. Zhang, R.-L. Zhong, M. Lu, J.-H. Wang, C. Jiang, G.-K. Gao, L.-Z. Dong, Y. Chen, S.-L. Li, Y.-Q. Lan, Single metal site and versatile transfer channel merged into covalent organic frameworks facilitate high-performance Li-CO_2 batteries. *ACS Cent. Sci.* **7**, 175–182 (2021).
39. P. A. Herrera-Herrera, E. Rodríguez-Sevilla, A. S. Varela, The role of the metal center on charge transport rate in MOF-525: Cobalt and nickel porphyrin. *Dalton Trans.* **50**, 16939–16944 (2021).
40. W.-J. Kwak, D. Hirshberg, D. Sharon, M. Afri, A. A. Frimer, H.-G. Jung, D. Aurbach, Y.-K. Sun, Li–O_2 cells with LiBr as an electrolyte and a redox mediator. *Energ. Environ. Sci.* **9**, 2334–2345 (2016).
41. T. Liu, M. Leskes, W. Yu, A. J. Moore, L. Zhou, P. M. Bayley, G. Kim, C. P. Grey, Cycling Li-O_2 batteries via LiOH formation and decomposition. *Science* **350**, 530–533 (2015).
42. D. Aurbach, B. D. McCloskey, L. F. Nazar, P. G. Bruce, Advances in understanding mechanisms underpinning lithium–air batteries. *Nat. Energy* **1**, 16128 (2016).
43. C. M. Burke, V. Pande, A. Khetan, V. Viswanathan, B. D. McCloskey, Enhancing electrochemical intermediate solvation through electrolyte anion selection to increase nonaqueous Li–O_2 battery capacity. *Proc. Natl. Acad. Sci. U.S.A.* **112**, 9293–9298 (2015).

44. K. U. Schwenke, M. Metzger, T. Restle, M. Piana, H. A. Gasteiger, The influence of water and protons on Li_2O_2 crystal growth in aprotic Li-O_2 cells. *J. Electrochem. Soc.* **162**, A573–A584 (2015).
45. H. Gao, B. M. Gallant, Advances in the chemistry and applications of alkali-metal–gas batteries. *Nat. Rev. Chem.* **4**, 566–583 (2020).
46. Z. Sun, C. Yang, F. Jiang, T. Zhang, Chimerism of carbon by ruthenium induces gradient catalysis. *Adv. Funct. Mater.* **31**, 2104011 (2021).
47. Y. Yang, T. Zhang, X. Wang, L. Chen, N. Wu, W. Liu, H. Lu, L. Xiao, L. Fu, L. Zhuang, Tuning the morphology and crystal structure of Li_2O_2: A graphene model electrode study for Li–O_2 battery. *ACS Appl. Mater. Interfaces* **8**, 21350–21357 (2016).
48. L.-N. Song, W. Zhang, Y. Wang, X. Ge, L.-C. Zou, H.-F. Wang, X.-X. Wang, Q.-C. Liu, F. Li, J.-J. Xu, Tuning lithium-peroxide formation and decomposition routes with single-atom catalysts for lithium–oxygen batteries. *Nat. Commun.* **11**, 2191 (2020).
49. L.-Z. Dong, Y. Zhang, Y.-F. Lu, L. Zhang, X. Huang, J.-H. Wang, J. Liu, S.-L. Li, Y.-Q. Lan, A well-defined dual Mn-site based metal–organic framework to promote CO_2 reduction/evolution in Li–CO_2 batteries. *Chem. Commun.* **57**, 8937–8940 (2021).
50. X. Mu, C. Xia, B. Gao, S. Guo, X. Zhang, J. He, Y. Wang, H. Dong, P. He, H. Zhou, Two-dimensional Mo-based compounds for the Li-O_2 batteries: Catalytic performance and electronic structure studies. *Energy Stor. Mater.* **41**, 650–655 (2021).
51. S. Yang, Y. Qiao, P. He, Y. Liu, Z. Cheng, J.-J. Zhu, H. Zhou, A reversible lithium–CO_2 battery with Ru nanoparticles as a cathode catalyst. *Energ. Environ. Sci.* **10**, 972–978 (2017).
52. G. Kresse, J. Furthmüller, Efficient iterative schemes for *ab initio* total-energy calculations using a plane-wave basis set. *Phys. Rev. B* **54**, 11169–11186 (1996).
53. G. Kresse, J. Furthmüller, Efficiency of ab-initio total energy calculations for metals and semiconductors using a plane-wave basis set. *Comput. Mater. Sci.* **6**, 15–50 (1996).
54. J. P. Perdew, K. Burke, M. Ernzerhof, Generalized gradient approximation made simple. *Phys. Rev. Lett.* **77**, –3865 (1997).
55. S. Grimme, J. Antony, S. Ehrlich, H. Krieg, A consistent and accurate *ab initio* parametrization of density functional dispersion correction (DFT-D) for the 94 elements H-Pu. *J. Chem. Phys.* **132**, 154104 (2010).
56. S. Grimme, S. Ehrlich, L. Goerigk, Effect of the damping function in dispersion corrected density functional theory. *J. Comput. Chem.* **32**, 1456–1465 (2011).
57. Y. Zhou, Q. Gu, K. Yin, Y. Li, L. Tao, H. Tan, Y. Yang, S. Guo, Engineering e_g orbital occupancy of Pt with Au alloying enables reversible Li–O_2 batteries. *Angew. Chem. Int. Ed.* **61**, e202201416 (2022).
58. L. Leng, J. Li, X. Zeng, H. Song, T. Shu, H. Wang, S. Liao, Enhancing the cyclability of Li–O_2 batteries using PdM alloy nanoparticles anchored on nitrogen-doped reduced graphene as the cathode catalyst. *J. Power Sources* **337**, 173–179 (2017).
59. T. Zhang, B. Zou, X. Bi, M. Li, J. Wen, F. Huo, K. Amine, J. Lu, Selective growth of a discontinuous subnanometer Pd film on carbon defects for Li–O_2 batteries. *ACS Energy Lett.* **4**, 2782–2786 (2019).
60. Y. Zhou, K. Yin, Q. Gu, L. Tao, Y. Li, H. Tan, J. Zhou, W. Zhang, H. Li, S. Guo, Lewis-acidic PtIr multipods enable high-performance Li–O_2 batteries. *Angew. Chem. Int. Ed.* **60**, 26592–26598 (2021).
61. S. Ma, Y. Wu, J. Wang, Y. Zhang, Y. Zhang, X. Yan, Y. Wei, P. Liu, J. Wang, K. Jiang, S. Fan, Y. Xu, Z. Peng, Reversibility of noble metal-catalyzed aprotic Li-O_2 batteries. *Nano Lett.* **15**, 8084–8090 (2015).
62. W.-B. Jung, H. Park, J.-S. Jang, D. Y. Kim, D. W. Kim, E. Lim, J. Y. Kim, S. Choi, J. Suk, Y. Kang, I.-D. Kim, J. Kim, M. Wu, H.-T. Jung, Polyelemental nanoparticles as catalysts for a Li–O_2 battery. *ACS Nano* **15**, 4235–4244 (2021).
63. B. Sun, S. Chen, H. Liu, G. Wang, Mesoporous carbon nanocube architecture for high-performance lithium–oxygen batteries. *Adv. Funct. Mater.* **25**, 4436–4444 (2015).
64. S. Wu, D. Wu, D. Zhang, W. Liu, H. Luo, J. He, Q. Yang, Z. Li, R. Liu, Boosting the activity and stability with dual-metal-N couplings for Li–O_2 battery. *Energy Environ. Mater.* **5**, 918–927 (2022).
65. J. Lu, S. Dey, I. Temprano, Y. Jin, C. Xu, Y. Shao, C. P. Grey, Co_3O_4-catalyzed LiOH chemistry in Li–O_2 batteries. *ACS Energy Lett.* **5**, 3681–3691 (2020).
66. K. R. Yoon, K. Shin, J. Park, S.-H. Cho, C. Kim, J.-W. Jung, J. Y. Cheong, H. R. Byon, H. M. Lee, I.-D. Kim, Brush-like cobalt nitride anchored carbon nanofiber membrane: Current collector-catalyst integrated cathode for long cycle Li–O_2 batteries. *ACS Nano* **12**, 128–139 (2018).
67. J.-J. Xu, Z.-W. Chang, Y. Wang, D.-P. Liu, Y. Zhang, X.-B. Zhang, Cathode surface-induced, solvation-mediated, micrometer-sized Li_2O_2 cycling for Li-O_2 batteries. *Adv. Mater.* **28**, 9620–9628 (2016).
68. B. He, G. Li, J. Li, J. Wang, H. Tong, Y. Fan, W. Wang, S. Sun, F. Dang, $MoSe_2$@CNT core–shell nanostructures as grain promoters featuring a direct Li_2O_2 formation/decomposition catalytic capability in lithium-oxygen batteries. *Advanced Energy Materials* **11**, 2003263 (2021).
69. M. Salehi, Z. Shariatinia, An optimization of MnO_2 amount in CNT-MnO_2 nanocomposite as a high rate cathode catalyst for the rechargeable Li-O_2 batteries. *Electrochim. Acta* **188**, 428–440 (2016).
70. J. Li, C. Shu, C. Liu, X. Chen, A. Hu, J. Long, Rationalizing the effect of oxygen vacancy on oxygen electrocatalysis in Li–O_2 battery. *Small* **16**, 2001812 (2020).
71. X. Lu, Y. Yin, L. Zhang, L. Xi, S. Oswald, J. Deng, O. G. Schmidt, Hierarchically porous Pd/NiO nanomembranes as cathode catalysts in Li-O_2 batteries. *Nano Energy* **30**, 69–76 (2016).
72. Q. Lv, Z. Zhu, Y. Ni, J. Geng, F. Li, Spin-state manipulation of two-dimensional metal–organic framework with enhanced metal–oxygen covalency for lithium-oxygen batteries. *Angew. Chem. Int. Ed.* **61**, e202114293 (2022).
73. X.-G. Wang, Z. Zhang, Q. Zhang, C. Wang, X. Zhang, Z. Xie, Z. Zhou, $MoCl_5$ as a dual-function redox mediator for Li–O_2 batteries. *J. Mater. Chem. A* **7**, 14239–14243 (2019).

Acknowledgments

Funding: This work was supported by the National Key Research and Development Program of China (2018YFA0306004 and 2019YFC0408303), the National Natural Science Foundation of China (nos. 21875099, 22033004, 21873045, 21922508, 22179059, and U1801251), and the Natural Science Foundation of Jiangsu Province (BK20220765 and BK20220928). We are grateful to the High Performance Computing Centre of Nanjing University for providing the IBM Blade cluster system. **Author contributions:** The original idea was conceived by J.-L.Z., P.H., S.Y., and J.M.; experiments and data analysis were performed by S.-W.K., W.L., Y.G., J.S., and Y.L.; structure characterization was performed by S.-W.K.; W.L. conducted the Li-O_2 cell performance; Y.G. performed the DFT calculations; and the manuscript was drafted by J.-L.Z., P.H., J.M., S.-W.K., W.L., Y.G., and S.Y. All authors have approved the manuscript. **Competing interests:** The authors declare that they have no competing interests. **Data and materials availability:** All data needed to evaluate the conclusions in the paper are present in the paper and/or the Supplementary Materials.

Submitted 7 October 2022
Accepted 30 December 2022
Published 1 February 2023
10.1126/sciadv.adf2398